molecular pharmaceutics

Article

Cite This: Mol. Pharmaceutics XXXX, XXX, XXX−XXX

Protein Adsorption and Layer Formation at the Stainless Steel−Solution Interface Mediates Shear-Induced Particle Formation for an IgG1 Monoclonal Antibody

Cavan K. Kalonia,[†,‡] Frank Heinrich,[§,∥] Joseph E. Curtis,[§] Sid Raman,[‡] Maria A. Miller,[‡] and Steven D. Hudson*[,†]

[†]Material Measurement Laboratory, National Institute of Standards and Technology (NIST), Gaithersburg, Maryland 20899, United States

[‡]Formulation Sciences Department, MedImmune Inc., Gaithersburg, Maryland 20878, United States

[§]NIST Center for Neutron Research, National Institute of Standards and Technology, Gaithersburg, Maryland 20899, United States

[∥]Department of Physics, Carnegie Mellon University, Pittsburgh, Pennsylvania 15213, United States

Supporting Information

ABSTRACT: Passage of specific protein solutions through certain pumps, tubing, and/or filling nozzles can result in the production of unwanted subvisible protein particles (SVPs). In this work, surface-mediated SVP formation was investigated. Specifically, the effects of different solid interface materials, interfacial shear rates, and protein concentrations on SVP formation were measured for the National Institute of Standards and Technology monoclonal antibody (NISTmAb), a reference IgG1 monoclonal antibody (mAb). A stainless steel rotary piston pump was used to identify formulation and process parameters that affect aggregation, and a flow cell (alumina or stainless steel interface) was used to further investigate the effect of different interface materials and/or interfacial shear rates. SVP particles produced were monitored using flow microscopy or flow cytometry. Neutron reflectometry and a quartz crystal microbalance with dissipation monitoring were used to characterize adsorption and properties of NISTmAb at the stainless steel interface. Pump/shear cell experiments showed that the NISTmAb concentration and interface material had a significant effect on SVP formation, while the effects of interfacial shear rate and passage number were less important. At the higher NISTmAb concentrations, the adsorbed protein became structurally altered at the stainless steel interface. The primary adsorbed layer remained largely undisturbed during flow, suggesting that SVP formation at high NISTmAb concentration was caused by the disruption of patches and/or secondary interactions.

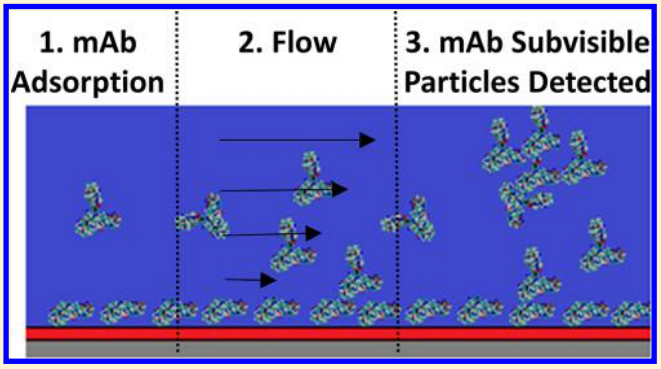

KEYWORDS: *monoclonal antibody, protein adsorption, subvisible particles, solid−liquid interface, protein aggregation, bioprocess development*

INTRODUCTION

Throughout biomanufacturing and storage, therapeutic protein solutions encounter many different interfaces (e.g., with air, silicone oil, stainless steel, alumina, and/or borosilicate glass), which can facilitate degradation pathways such as non-native aggregation.[1] Non-native aggregation (hereafter referred to as aggregation) mechanisms initiated at the air−solution interface[2−5] and the silicone oil−solution interface[6−9] have received substantial attention and are often related to compression or physical disruption of the interface. Protein often adsorbs to, and concentrates at, these phase boundaries, which may result in conformational changes and/or clustering of protein at the interface. Interfacial stress (e.g., dilatational or planar compression) may eject particles and/or their nuclei into solution.[2,4] Degradation pathways involving solid−liquid interfaces[10−13] have also been studied but remain poorly understood. Such mechanisms, however, are important to understand because solid interfaces that contact solution (e.g., borosilicate glass, alumina, stainless steel) are present after the final filtration step during fill/finish (e.g., filling nozzle and drug product container closure). Thus, aggregates produced by mechanisms involving the solid−liquid interface remain in the drug product.

Aggregates and subvisible particles (large aggregates with dimensions between 1 and 100 μm) that form during fill/finish,

Received: December 13, 2017
Revised: February 5, 2018
Accepted: February 9, 2018
Published: February 9, 2018

© XXXX American Chemical Society

DOI: 10.1021/acs.molpharmaceut.7b01127
Mol. Pharmaceutics XXXX, XXX, XXX−XXX

storage, shipping, and/or administration could be injected into patients. A commentary published in 2009 by Carpenter et al. asserted that submicron and subvisible particles were particularly important to monitor and control for safety and efficacy reasons.[14] Since this time, a number of studies have been published that demonstrate that highly aggregated protein products may enhance immunogenicity compared to native protein products.[15−18] These studies, however, also suggest that (1) not all populations of subvisible protein particles (SVPs) elicit or enhance immunogenicity and (2) the numbers of subvisible particles required to elicit or enhance immunogenicity is quite high (e.g., much greater than what is commonly found in marketed products). Despite the uncertain link between SVPs and immunogenicity, regulatory agencies such as the U.S. Food and Drug Administration have increasingly been requesting SVP data from biopharmaceutical companies as part of the application process. Therefore, understanding protein aggregation facilitated by solid−liquid interfaces is of interest to better understand the effects of different control strategies on mitigating such aggregation mechanisms.

Protein adsorption to solid interfaces may result in cluster formation (reversibly or irreversibly associated protein) and/or conformational perturbations.[19−21] Langdon et al. showed that cluster associations increased for bovine serum albumin on a polyethylene glycol functionalized silica substrate with increasing protein concentration.[19] Protein clusters and/or partially unfolded protein molecules are often susceptible to aggregate growth and nucleation mechanisms in bulk solution.[22−24] Presumably, such nucleation and growth mechanisms could also occur at the solid interface; however, such mechanisms have not been demonstrated or modeled at the interface. It is also not well understood how additional factors such as flow (shear at the interface) affect interface-mediated protein aggregation and SVP formation.

In this work, the effect of monoclonal antibody (mAb) concentration on mAb adsorption to stainless steel was investigated. Additionally, the effect of flow (interfacial shear) past mAb adsorbed to stainless steel on SVP formation was elucidated for solutions of NISTmAb. To investigate the physical properties of the adsorbed mAb including conformation, orientation, layer thickness, and viscoelasticity, we used a combination of a quartz crystal microbalance with dissipation monitoring and neutron reflectometry. The effects of different interfaces and flows on particle formation were investigated using an in-house shear cell and a stainless steel rotary piston pump. Aggregates generated from the shear/pump studies were characterized using size exclusion chromatography and particle counting techniques. Interface material had a profound effect on SVP formation for this mAb. Additionally, increasing the mAb concentration, shear rate, and/or passage number (in a rotary piston pump or flow cell) also increased the number of SVPs in solution for certain interface materials, suggesting that mAb adsorption at the solid−liquid interface and interfacial shear may play critical roles in SVP formation during biopharmaceutical fill/finish operations.

EXPERIMENTAL PROCEDURES

Materials. The NIST monoclonal antibody (NISTmAb), an IgG1 mAb reference material, was provided frozen at −80 °C by NIST at a concentration of 100 g/L in pH 6.0, 25 mmol/L histidine buffer.[25] L-histidine and L-histidine hydrochloride (J.T. Baker Chemical Co., Phillipsburg, New Jersey) were used to prepare additional pH 6.0, 25 mmol/L histidine buffer. The stock solution of NISTmAb was diluted to concentrations of (0.1, 10, 25, 50) g/L and sterile filtered. D_2O (Cambridge Isotope Laboratories Inc., Andover, Massachusetts) was used to prepare pD 6.0, 25 mmol/L histidine buffer. NISTmAb was exchanged into D_2O buffer using 30 kDa NMWL Amicon Ultra-15 centrifugal filter units (EMD Millipore Co, Billerica, Massachusetts). The retentate was exchanged 3× and sterile filtered. The concentration of mAb in the D_2O exchanged and diluted H_2O solutions was measured using UV−vis absorbance spectroscopy ($\epsilon^{0.1\%}_{280\,nm}$ = 1.4 $L{\cdot}g^{-1}$ cm^{-1}) and adjusted if necessary. The 60% D_2O buffer protein solutions were prepared by mixing protein solutions prepared in D_2O and H_2O.

Silicon wafers coated with stainless steel or alumina (layer ≈ 15 nm thick) were prepared by the NanoFab group, part of the Center for Nanoscale Science and Technology at NIST. The 316L stainless steel target was purchased from ACI alloys Inc. (San Jose, California). The quality and reusability of the coated wafers were checked using X-ray reflectivity (see the Supporting Information).

Rotary Piston Pump Experiment. A 316L stainless steel rotary piston pump (part # 46240456, Bausch & Ströbel, Ilshofen, Germany) with an FSR1000 rotary piston pump driver (Colanar Inc., Deep River, Connecticut) was used to investigate the effect of NISTmAb concentration on SVP formation during fill/finish unit operations. The pump was set to dispense 1 mL per stroke and was operated at a rate of ∼30 strokes/min. A 25 mL sample reservoir was used to recirculate NISTmAb solution through the pump until the total number of strokes was equal to 1, 5, 10, or 20 passes on a volume-averaged basis. Rotary piston pump experiments were performed for NISTmAb concentrations of 10, 25, 50, and 100 g/L.

Flow Cytometry. A customized BD LSRII flow cytometer (BD Biosciences, San Jose, California) with a 488 nm laser was used to count SVPs generated during the rotary piston pump study. SVP were counted using forward and side scattering detectors with a minimal trigger threshold. Sample (150 μL) was added to a 96-well plate, and 50 μL from each well was mixed and injected at a flow rate of 0.5 μL/s. The instrument was washed between samples to prevent carryover. Buffer control experiments were performed to ensure instrument cleanliness. Six measurements were performed for each pump experiment. Uncertainties reported are one standard deviation from the mean of the repeated measurements.

Neutron Reflectometry. The CGD-MAGIK off-specular reflectometer at the NIST Center for Neutron Research (NCNR) was used for neutron reflectometry experiments.[26] Measurements were performed using the standard flow cell configuration available at the NCNR.[27] The flow cell was assembled with a silicon wafer that had been sputter-coated using a 316L stainless steel target. Figure 1A is a schematic representation of the experimental neutron reflectometry configuration using the flow cell. Specular reflection was measured over a momentum transfer (Q_z) range of 0.008−0.250 $Å^{-1}$ with most data points collected between (0.008 and 0.120) $Å^{-1}$. Counting times for each data point were weighted with respect to Q_z (counting times were highest for high Q_z values). The total time to collect a single reflectivity curve was approximately 6.5 h.

Experiments were sequentially performed using in situ solvent exchanges with pure buffer, 0.1 g/L NISTmAb, 50 g/L NISTmAb, and 100 g/L NISTmAb. Two isotopic contrasts of 100% H_2O buffer and 100% D_2O buffer were used for the

DOI: 10.1021/acs.molpharmaceut.7b01127
Mol. Pharmaceutics XXXX, XXX, XXX−XXX

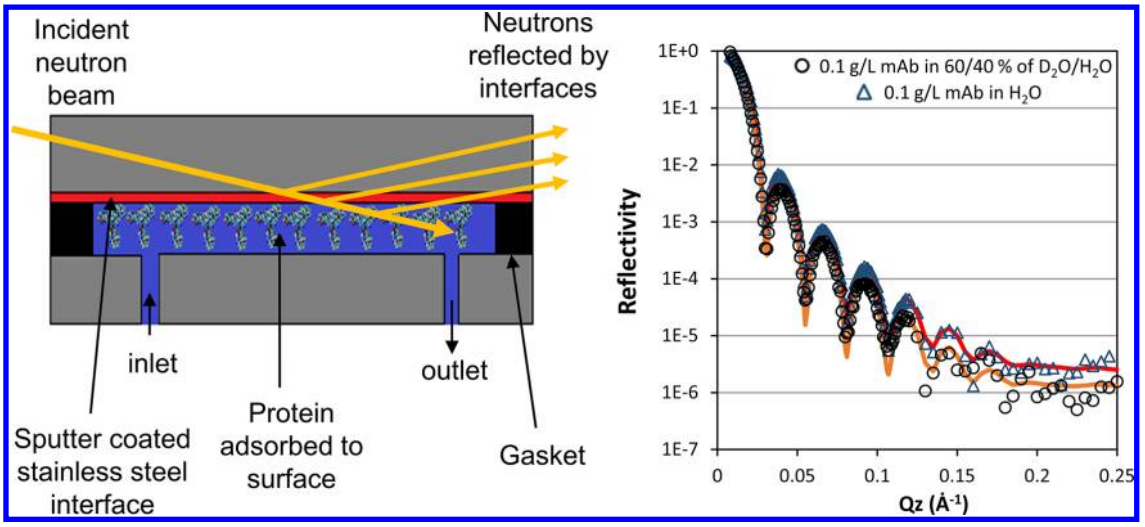

Figure 1. Neutron reflectivity measured in a flow cell with a stainless steel interface. (Left) Schematic representation of the flow cell and experimental setup. The schematic depicts a collimated neutron beam and reflected neutrons for a single wave vector (Q_z). Neutrons reflect from the different interfaces in the system including the Si wafer/stainless steel, stainless steel/mAb, and mAb/solution interfaces. Interference between the neutrons reflected from the different interfaces give rise to oscillations in the reflectivity. (Right) Reflectivity data for a flow cell with a stainless steel interface that was filled with a 0.1 g/mL mAb solution. The circles are experimental data points for 0.1 g/L mAb in a 60/40% blend of D_2O/H_2O buffers. The blue triangles are experimental data points for 0.1 g/L mAb in a H_2O buffer. The red and orange traces are the best simultaneous fit of the data. The fit provides structural information about the adsorbed mAb layer including the thickness and volume fraction.

specular reflection and background measurements of the substrate. For the mAb solutions, 100% H_2O buffer and a 60/40% mixture of D_2O and H_2O histidine buffers were used. Data reduction was performed using Reductus software (https://www.nist.gov/ncnr/reflectometry-software) developed at the NCNR.

The neutron reflectivity data was analyzed to obtain a 1D scattering length density profile normal to the substrate surface. Neutron reflectometry averages in planes orthogonal to this direction. A slab model was used to parametrize the substrate to account for the bulk silicon, silicon oxide, and stainless steel layers.[28] Parameters for the slab model were the neutron scattering length density (nSLD) and thickness for each layer and global roughness. A Hermite spline was used to parametrize the adsorbed mAb layer(s) in terms of nSLD and thickness.[29] Experimental reflectivity data at both isotopic contrasts were simultaneously fit using *ga_refl*[30] and *refl1D* software, using a Monte Carlo Markov chain-based global optimizer that yields accurate confidence intervals on all fit parameters.[27]

Quartz Crystal Microbalance. A Q-Sense E4 (Biolin Scientific Holding AB., Stockholm, Sweden) was used to perform up to four simultaneous quartz crystal microbalance with dissipation monitoring (QCM-D) measurements. QSoft401 v2.5.20.690 software (Biolin Scientific Holding AB.) was used to monitor the fundamental resonant frequency and dissipation factor of the quartz crystal. Frequency and dissipation factor values were also monitored for the 3rd, 5th, 7th, 9th, 11th, and 13th overtones. Experiments were performed using stainless steel (SS2343) or aluminum oxide sensors purchased from Biolin Scientific Holding AB. SS2343 grade stainless steel sensor was used because the composition of SS2343 is nearly identical to the composition of 316L grade stainless steel.[31]

QCM-D experiments were performed as a series of sequential steps: (1) a buffer baseline was measured, (2) a mAb solution was introduced into the flow cell, and (3) the flow cell was rinsed with buffer. Frequency and dissipation factor values were established for the sensor in a dry flow cell. The sample reservoir was changed to buffer, and the flow rate was set to 50 μL/min. After ~1 h of continuous buffer flow through the flow cell, the experiment was started. After a ~5 min acquisition time for the buffer baseline, the sample reservoir was changed to a mAb solution. Upon observing a change in frequency and waiting approximately 60 s, the flow rate was decreased to 10 μL/min. Data for the mAb solution was acquired for approximately 30 min or until the normalized frequency shift changed by less than 1 Hz/10 min. After sufficient data collection for the mAb solution, the sample reservoir was changed to buffer and the flow rate was increased to 500 μL/min. The flow cell was rinsed with buffer for at least 30 min. Experiments were performed with mAb concentrations of 0.1, 10, 50, and 100 g/L for both the stainless steel and alumina coated sensors.

The frequency and dissipation values for the quartz oscillator will shift if there is a change in the density or viscosity of the sensor environment (e.g., the solution). Kanazawa et al. have shown this frequency shift to be

$$\Delta f_n = -n^{1/2} f_o^{3/2} \sqrt{\frac{\rho_{liq}\eta_{liq}}{\pi\rho_q\mu_q}} \quad (1)$$

for a quartz disk initially exposed to a vacuum and then to a viscous liquid.[32] Here, Δf_n is the frequency shift, n is the overtone number, f_o is the fundamental frequency, ρ_{liq} is the density of the solution, η_{liq} is the viscosity of the solution, ρ_q is the density of quartz (2650 kg/m^3), and μ_q is the elastic modulus of the stiffened quartz (2.947×10^{10} Pa).[33] The corresponding dissipation shift for the quartz oscillator is

$$\Delta D_n = 2n^{-1/2} \sqrt{\frac{f_o\rho_{liq}\eta_{liq}}{\pi\rho_q\mu_q}} \quad (2)$$

DOI: 10.1021/acs.molpharmaceut.7b01127
Mol. Pharmaceutics XXXX, XXX, XXX−XXX

for a transition from a vacuum to a viscous Newtonian fluid.[34,35] For reference, these shifts in water at 23 °C are $-690n^{1/2}$ and $2.8 \times 10^{-4}n^{-1/2}$ for the frequency and dissipation shifts, respectively.

If molecules adsorb to the surface of the sensor and the solution environment stays constant, the frequency and dissipation values for the sensor will shift based on the physical properties of the adsorbed layer (e.g., thickness, viscosity, shear modulus, and density). If the adsorbed layer is uniform, rigid (i.e., dissipation is negligible), and small relative to the mass of the sensor, the Sauerbrey equation

$$\Delta f_n = -\frac{2nf_o^2}{\rho_q v_q}\Delta m \tag{3}$$

can be applied to relate a frequency shift to a change in mass on the sensor.[36] Here, v_q is the shear wave velocity in quartz and Δm is the mass added to the sensor.[35] Rearranging eq 3, the normalized frequency shift ($\Delta f = \Delta f_n/n$) can be expressed as

$$\Delta f = C\Delta m \tag{4}$$

where $C = -\frac{2f_o^2}{\rho_q v_q} = -17.7$ cm^2/ng·s. The Sauerbrey model can be applied to QCM-D data when the dissipation factor is close to 0 and the normalized frequency shifts overlap.[35] Therefore, we applied the Sauerbrey model to analyze data collected during the buffer rinse step.

When the sensor is exposed to the antibody solution, the response is more complex. This is because at a minimum both adsorption and a change in solution viscosity occur. A two-layer Voigt model, implemented in QTools 3 software (Biolin Scientific Holding AB.), was used to analyze the data acquired during the last 20 min of the mAb adsorption step. This model was selected to account for the change in solution viscosity (buffer to protein solution) *and* reversible layer formation. Simpler models were not able to fit the data (e.g., Sauerbrey and one-layer Voigt). For a detailed derivation and explanation of the two-layer model, please refer to Voinova et al.[37] The solution viscosity was measured (see the Results section), and the solution density, layer 1 (L1) density, and layer 2 (L2) density were set as user-defined constants. The other parameters (including thickness, viscosity, and shear modulus for L1 and L2) were optimized by the software to achieve the best possible simultaneous fit of the frequency and dissipation shifts for the 3rd, 5th, 7th, 9th, 11th, and 13th overtones. Given the large number of fit parameters, a number of parameter combinations were possible to fit the data; therefore, we report the best fit values (lowest χ^2) and the range for each parameter (with other parameters allowed to vary) for which χ^2 is less than double that of the best fit.

The complex modulus is $G^* = G' + iG'' = G' + i\omega\eta'$, where G' is the storage modulus (also referred to as the shear modulus), G'' is the loss modulus, ω is the angular frequency, and η' is the viscosity. The two-layer Voigt model provides G' and η' as output parameters. Using these values, we can calculate $\tan(\delta)$ to determine whether the layers exhibit solid-like or liquid-like behavior

$$\tan(\delta) = \frac{G''}{G'} = \frac{\omega\eta'}{G'} \tag{5}$$

For calculations using eq 5, we used the third overtone (15 MHz) to calculate the angular frequency. When $\tan(\delta) > 1$, the layer exhibits more liquid-like behavior, and when $\tan(\delta) < 1$, the layer exhibits more solid-like behavior at the corresponding ω.

Viscometry. An m-VROC viscometer (RheoSense, San Ramon, California) was used to measure the viscosity as a function of shear rate. Prior to measurement, the syringe and chip were cleaned using a 1% bleach solution, isopropanol, and water. The viscosity of the 0.1 and 10 g/L NISTmAb solutions was measured using the "B" chip over a range of shear rates from 7000 to 70 000 s^{-1}. The viscosity of 50 and 100 g/L NISTmAb solutions was measured using the "C" chip over the same range of shear rates. A total of three experiments were performed for each protein concentration.

Shearing Experiment to Investigate SVP Formation during Flow. The neutron reflectivity flow cell was assembled using either the alumina or stainless steel coated substrates (Figure 1A). The cell was slowly filled with NISTmAb solution and allowed to incubate at room temperature for 30 min. During this time, the inlet and outlet ports were closed to prevent exposure to air. A syringe filled with 1 mL of NISTmAb solution was added to the sample inlet port, and an empty syringe was added to the outlet port. Using the dual syringe setup, the NISTmAb solution was sheared back and forth 3× (one way) at a flow rate of 0.1, 2, or 120 mL/min through the flow cell assembled with the stainless steel substrate with minimal quiescent time (<10 s) between each passage. NISTmAb solutions were also sheared back and forth 10× (one way) at a flow rate of 120 mL/min through the flow cell assembled with the alumina substrate and stainless steel substrate. A total of three replicates were performed at each condition with the flow cell cleaned between each replicate. The stainless steel substrates were reused after cleaning because the structure of the coating did not change after cleaning. Alumina substrates, on the other hand, were not reused because the structure of the coating changed after being cleaned with detergent. Shearing experiments were performed using NISTmAb concentrations of 0.1, 50, and 100 g/L.

Wall shear rates were calculated for pressure-driven flow through a rectangular pipe

$$g = \frac{6Q}{wh^2} \tag{6}$$

where g is the wall shear rate, Q is the volumetric flow rate, w is the channel width, and h is the channel height. Because the base of the flow cell was circular, the value of w was approximated as a chord across the circle based on the position in the flow cell. Median wall shear rates are reported for each experiment: 20, 400, and 25 000 s^{-1}. No visible air bubbles were observed in the recovered sample.

Subvisible Particle Detection. A DPA 5200 Microflow Imaging (MFI) system (Protein Simple, San Jose, California) was used to count and size SVPs from 2 to 100 μm equivalent circular diameter (ECD) in size produced during the shearing experiments. Then, 200 μL of sample was used to purge the MFI flow cell and 600 μL of sample was used for analysis. Buffer and unstressed mAb controls were used to ensure instrument and sample cleanliness (prior to shearing experiments). To reduce undercounting caused by low contrast between particles and the background solution, samples with >10 g/L NISTmAb concentration were diluted to 10 g/L.[38] The reported SVP counts were corrected by a dilution factor.

DOI: 10.1021/acs.molpharmaceut.7b01127
Mol. Pharmaceutics XXXX, XXX, XXX−XXX

RESULTS

Flow- and Interface-Mediated Subvisible Particle Formation. A stainless steel rotary piston pump (SS-RPP) produced SVPs depending on the mAb solution concentration. At low mAb concentration (e.g., 10 g/L), there was a large initial increase in the total SVP concentration after one pump passage (Figure 2). Subsequent passages, however, did not have much effect on the total SVP population (Figure S1). Interestingly, increasing the mAb solution concentration caused more SVP to be produced after the initial pump passage and during subsequent passages. The amount of SVP produced after the initial passage, however, was much greater than the amount produced by any subsequent pump passage (Figures 2, S1). Figure 2 demonstrates that the effect of mAb solution concentration on pump-induced SVP formation was greatest when increasing from low mAb solution concentrations (e.g., 10 g/L) to intermediate concentrations (e.g., 50 g/L). Increasing from an intermediate mAb solution concentration (e.g., 50 g/L) to a high concentration (e.g., 100 g/L) did not have a substantial effect because one pump passage produced similar numbers of particles for both concentrations. Additionally, subsequent pump passages produced similar numbers of SVPs/passage (approximated using a linear fit) for the 50 and 100 g/L mAb solutions (Figure S1). The SS-RPP represents a complex system with many different factors that could contribute to SVP formation (e.g., grinding of piston against wall, interfacial shear, cavitation, etc.). Therefore, a flow cell was used for all further studies to specifically investigate the effect of interfacial shear and different interface materials on SVP formation for this mAb.

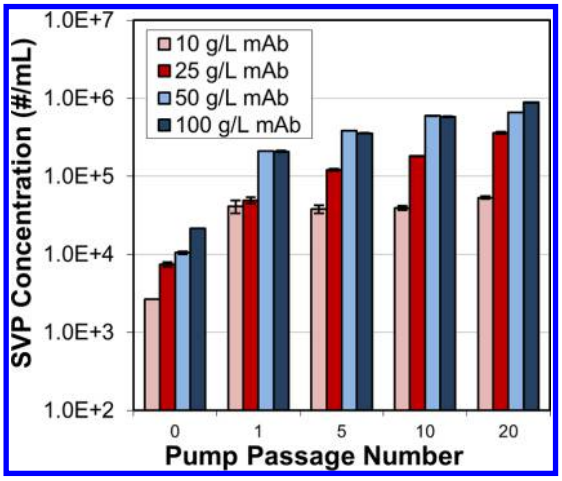

Figure 2. Concentration of subvisible particles detected after passage of NISTmAb solutions through a stainless steel rotary piston pump. The light red, dark red, light blue, and dark blue bars represent NISTmAb solutions formulated at 10, 25, 50, and 100 g/L, respectively. Uncertainties denote the standard error of the mean calculated from six measurements of the pumped solution. SVPs were counted using flow cytometry.

In the shearing flow cell, different solid interfaces were tested so that all other process conditions could be compared consistently. To test various hypotheses, 1-tailed *t* tests with a 0.10 significance level were performed for different concentrations (H_1 = increasing concentration produces more particles) and different interfaces (H_1 = stainless steel interfaces produce more SVPs than alumina interfaces). After 10 passages at a flow rate of 120 mL/min (interfacial shear rate of 25 000 s^{-1}), the number of particles produced in the flow cell with the stainless steel interface was not significantly different from the alumina interface for the 0.1 g/L mAb solution (Figure 3A). As the mAb concentration was increased, the number of SVPs did not increase much for solutions exposed to the alumina interface and high shear. A linear function was used to quantitatively estimate the effect of protein concentration (ranging from 0.1 to 100 g/L) on SVP formation. The fit of SVP formation after fast flow past the alumina interface (Figure

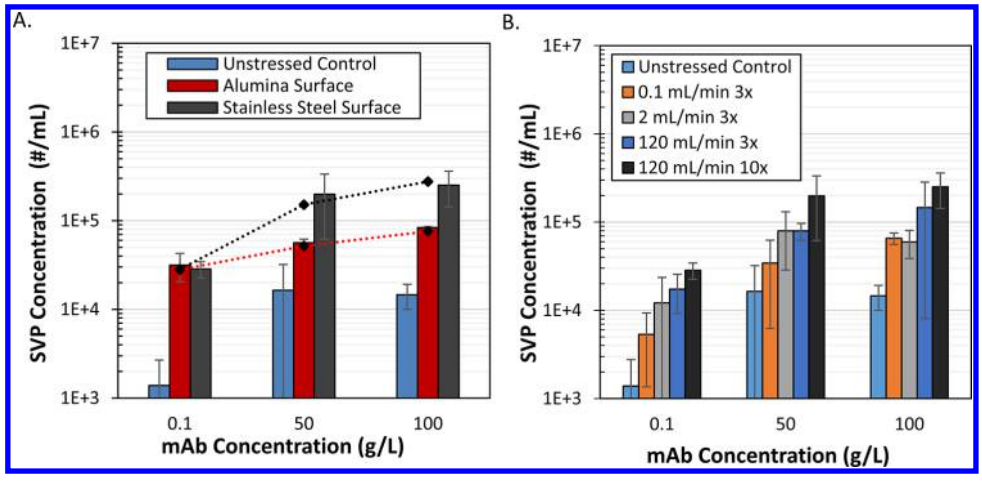

Figure 3. Concentration of subvisible particles detected after passage of NISTmAb solutions through a flow cell with different interface materials or at different flow rates. The total concentration of SVP ≥ 2 μm in stressed and unstressed NISTmAb solutions was counted using MFI. Error bars denote the standard deviation of three separate experiments. (A) Effect of alumina (red bar) and 316L stainless steel (dark gray bar) interfaces on SVP formation during shear. SVPs were measured after 10× passes through a flow cell at 120 mL/min. Stressed particle numbers were compared to an unstressed control (blue bar). The black diamond points of the dashed black line represent a linear increase in particle formation of 2472 × mAb concentration + 28 000 particles. The black diamond points of the dashed red line represent a linear increase in particle formation of 477 × mAb concentration + 28 000 particles. (B) Effect of different flow rates and number of passages through a flow cell with a 316L stainless steel interface on SVP formation. SVPs were counted for samples recovered after 3× passes through the flow cell at 0.1 (orange bar), 2 (light gray bar), and 120 mL/min (dark blue bar) flow rates. SVPs were also counted after 10× passes at 120 mL/min (black bar) and for an unstressed control (light blue bar).

DOI: 10.1021/acs.molpharmaceut.7b01127
Mol. Pharmaceutics XXXX, XXX, XXX−XXX

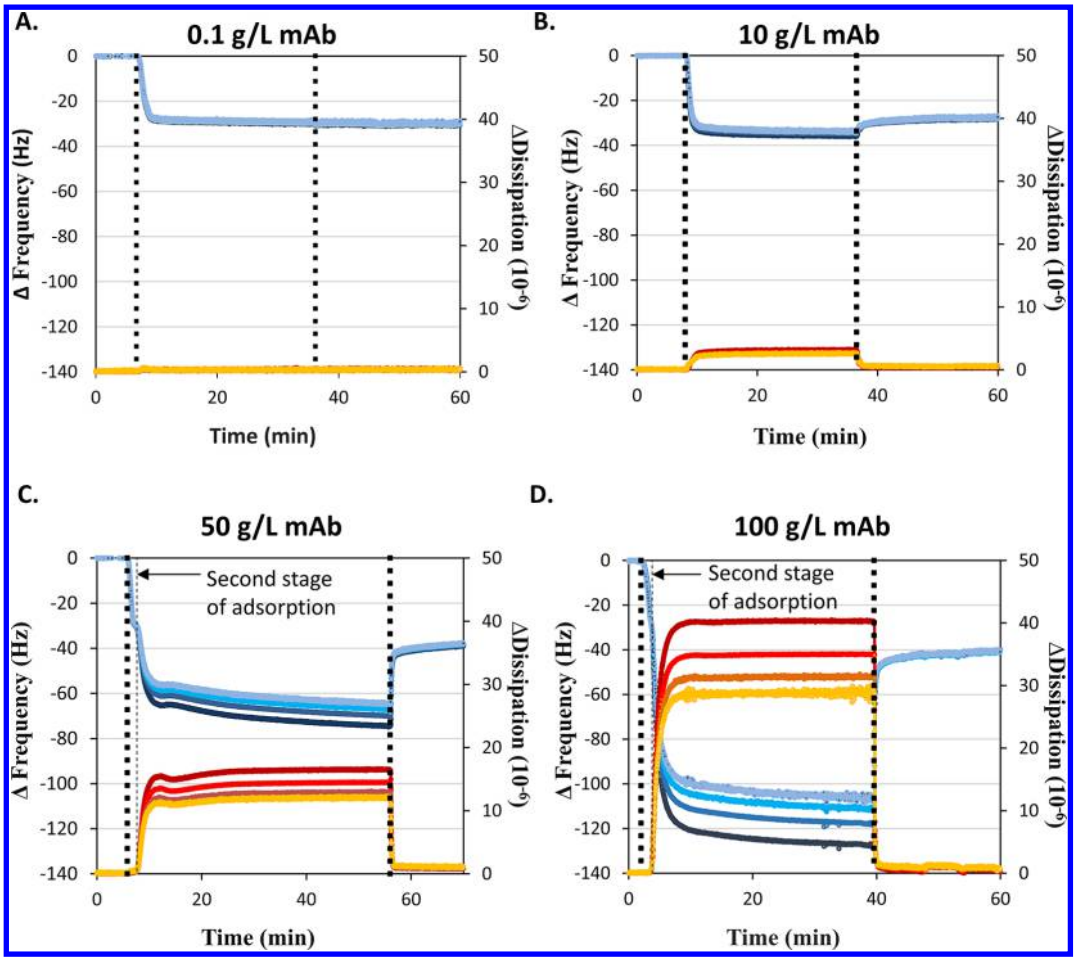

Figure 4. Normalized frequency and dissipation shifts measured using a quartz crystal microbalance with dissipation monitoring. QCM-D data acquired as a three-step experiment involving (1) flow of buffer to establish a baseline, (2) flow of mAb solution to monitor adsorption, and (3) fast flow of buffer as a rinsing step. Transitions between steps are marked using bold dashed vertical lines. The lighter dotted vertical lines in panels (C) and (D) mark the sharp rise in dissipation associated with a second stage of adsorption, which occurs at high protein concentration. The light orange, orange, red, and dark red traces represent the 13th, 11th, 9th, and 7th overtones of the fundamental dissipation shift, respectively. The blue colors represent the 13th (lightest blue), 11th (light blue), 9th (dark blue), and 7th (darkest blue) overtones of the fundamental frequency shift. Experiments were performed using a stainless steel sensor and (A) 0.1, (B) 10, (C) 50, and (D) 100 g/L mAb solutions.

3A) demonstrated that there was no substantial difference between the different concentrations (e.g, particles = 477 × protein concentration (g/L) + 28 000) tested. Despite the small differences between the different concentrations, the results were statistically significant. NISTmAb solutions exposed to stainless steel and high shear, on the other hand, produced substantially more SVPs as the concentration was increased (Figure 3A). As before, a linear function was used to quantitatively estimate the effect of protein concentration on SVP formation. The linear fit of SVP formation after fast flow past the stainless steel interface demonstrated that increasing mAb concentration caused substantially more particles to be produced (particles = 2472 × protein concentration + 28 000). The distribution of SVP size did not appear to be impacted notably by mAb concentration or interface material (Figure S2). Differences in SVP numbers were statistically significant between 0.1 and 50 or 100 g/L mAb solutions. Confidence intervals (95%) for the slope of SVP concentration vs mAb concentration fits for stainless steel and alumina interfaces can be found in Figure S3. These results demonstrate that a substantial portion of SVPs produced during shear are mediated by interactions with the solid interface because the stainless steel interface caused more SVP formation than the alumina interface as a function of mAb concentration.

To further investigate the effects of alumina vs stainless steel interfaces on SVP formation, several experiments were performed to determine whether these interfaces produce small, soluble mAb aggregates or shed interface material into solution (e.g., stainless steel particles). Size exclusion chromatography (SEC) was used to assess whether small aggregates were present in solution, and X-ray reflectivity was used to assess whether the interfaces remained stable (e.g., did not shed stainless steel particles, etc.). Comparing stressed samples with unstressed controls, the SEC results show no difference in the respective levels of soluble aggregates (dimers, trimers, etc.) for the 50 and 100 g/L NISTmAb produced at 20, 400, and 25 000 s^{-1} (Figure S4). X-ray reflectivity was performed on a stainless steel substrate that had been cleaned with detergent after a set of shearing experiments (Figure S5). The best fit of the data shows that the thickness of the stainless steel remained unchanged and that the density/surface roughness of the surface remained comparable to the original structure. Therefore, NISTmAb adsorption and interfacial shear did not damage the solid interface through the shedding of nm to μm sized particles.

DOI: 10.1021/acs.molpharmaceut.7b01127
Mol. Pharmaceutics XXXX, XXX, XXX−XXX

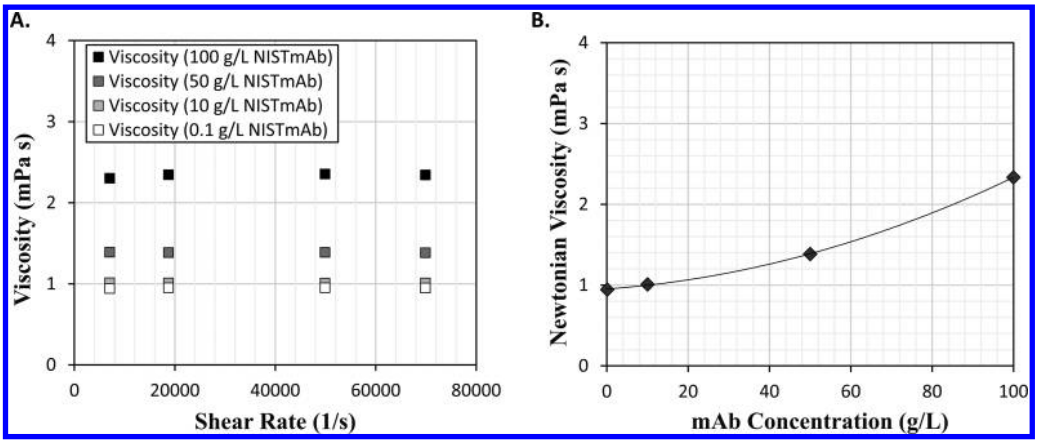

Figure 5. Viscosity of NISTmAb solutions. (A) Viscosity plotted as a function of shear rate. (B) Newtonian viscosity plotted as a function of NISTmAb concentration. Error bars, representing the standard deviation of three separate experiments, are smaller than the symbols representing the data points.

Different flow rates were used in the shearing flow cell, equipped with the stainless steel interface, to elucidate the effect of interfacial shear on SVP formation. Flow rates of 0.1, 2.0, and 120 mL/min (Figure 3B) corresponding to median interfacial shear rates of 20, 400, and 25 000 s^{-1} were used for these studies, respectively. As before, a 1-tailed t test with a 0.10 significance level was performed to test whether SVP populations were statistically different (H_1 = faster/longer flows produce more particles). In general, differences in SVP populations were not significant for the different flow rate experiments when the passage number was held constant at 3× (the exceptions being between 20 s^{-1} and 25 000 s^{-1} at 0.1 and 50 g/L NISTmAb, respectively. Additionally, differences in SVP numbers produced after 3× and 10× passages at 120 mL/min were not significant except at 0.1 g/L mAb with $p = 0.066$. No significant differences were observed in the SVP size distribution as a function of shear rate (Figure S6). These results suggest that while interfacial shear rate affects SVP formation it is not as important as the other variables investigated (e.g., mAb concentration and solid interface material) for the conditions tested in this study. As there was no significant impact across several orders of magnitude for interfacial shear rate, further intermediate points were not investigated.

Interface Properties and mAb Adsorption. The adsorption process was monitored dynamically by QCM-D (Figure 4) for mAb concentrations ranging from 0.1 to 100 g/L, using a stainless steel sensor to better understand how solution concentration affects interface-mediated SVP formation. A number of features are apparent in light of the various limits and conditions discussed in the Experimental Procedures section. First, at low concentration (0.1 g/L mAb), dissipation is minimal ($<5 \times 10^{-7}$) and the normalized frequency shift, Δf, overlaps for all of the different overtones. These features are within the Sauerbrey limit, which means that the adsorbed mAb layer is weakly coupled to the environment and therefore should be considered thin and rigid. At high concentration, adsorption occurred in a two-stage process. The first, rapid step appeared to be similar to the adsorption at low concentration: Δf was approximately −30 Hz and ΔD was $<5 \times 10^{-7}$ (Figure 4C,D). The second, subsequent adsorption step coincided with a dramatic rise in dissipation. In this step, there was a further decrease in Δf and overtone spreading was observed. Overtone spreading is expected whenever dissipation occurs (e.g., substantial solution viscosity or layer viscoelasticity). Finally, a small, transient peak followed by a dip in ΔD (and similarly Δf) was observed during the second stage, especially at intermediate concentrations (Figure 4C). This feature, predicted by Voinova et al.,[37] occurs when a viscoelastic layer grows while in contact with a viscous liquid. The structure and properties at high concentration are therefore considerably different.

Voinova's[37] two-layer Voigt model was selected to model adsorption and clustering interactions while the cell was filled with mAb solution because of the complexity of the high mAb concentration data, as described above. We denote the two layers as primary (L1, adjacent to the substrate) and secondary (L2, residing on L1 and forming only during the second stage of adsorption). At appropriate limits, this model conforms to either the Sauerbrey limit or the viscous medium limit (see methods section). At moderate to high mAb concentrations (≥10 g/L mAb), dissipation and overtone spreading was observed for the Δf and ΔD signals, as noted above. To accurately account for the effect of solution viscosity on the QCM-D signals, the solution viscosity parameter in the Voigt model was set to the experimentally measured bulk solution viscosity. Solution viscosity was measured as a function of shear rate in the absence of any air−solution interface (similar to the QCM-D flow cell). The measured viscosity was Newtonian over the measured shear rates from ∼7000 to 70 000 s^{-1} (Figure 5A). The Newtonian viscosity at 0.1, 10, 50, and 100 g/L mAb was 0.95, 1.05, 1.40, and 2.35 mPa s, respectively (Figure 5B). A single-layer model, which accounted for changes in solution viscosity, was unable to properly fit the data at moderate to high mAb concentrations of ≥10 g/L. In all cases, the two-layer model could adequately model the data. Solution density values for the 0.1, 10, 50, and 100 g/L mAb solutions were set to 1.000, 1.003, 1.015, and 1.030 g/mL, respectively, based on calculations using a mAb density of 1.42 g/cm^3 and a buffer density of 1.00 g/mL.[39] In rough accord with neutron reflectivity results presented below, the density of L1 was set to 1.126 g/mL (corresponding to 30% mAb volume fraction) and that of L2 was set to equal the solution density. These densities approximate a dense layer and a very loose layer, respectively. The resulting fit achieved low χ^2 values, and output values for the shear modulus of the primary L1 layer were of similar magnitude to a published value of ∼10 MPa for a another protein.[40] The parameters obtained from this model (e.g., shear

DOI: 10.1021/acs.molpharmaceut.7b01127
Mol. Pharmaceutics XXXX, XXX, XXX−XXX

modulus, layer thickness, and layer viscosity) were used to calculate the viscoelastic ratio, tan(δ), and the mass of protein contained within each layer to better compare the physical properties near the stainless steel interface for the different mAb solution concentrations.

The physical properties of the adsorbed primary layer, e.g., thickness and viscoelasticity, were sensitive to mAb concentration as determined by the two-layer Voigt model (Figure 6A). At 0.1 and 10 g/L mAb, the thickness of the primary layer, adsorbed to stainless steel, was ~5 nm under both solution conditions (Figure 6A). At 50 and 100 g/L, however, the modeled thickness of the primary layer increased slightly to ~6 and 8 nm, respectively. Protein mass was calculated by assuming that the primary layer was composed of 30% protein. The range of mass for the primary layer was ~210 to 340 ng/cm^2. Additionally, the total layer mass (not shown), calculated using a layer density of 1.126 g/mL, was in good agreement with Sauerbrey model results (see below). The change in the viscoelasticity of the primary layer correlated with the mAb concentration. Specifically, the tan(δ) value decreased from ~0.6 at 0.1 g/L mAb to <0.01 at 100 g/L mAb (Figure 6C). These results demonstrate that the primary layer became slightly thicker and increasingly more solid-like as the mAb solution concentration was increased.

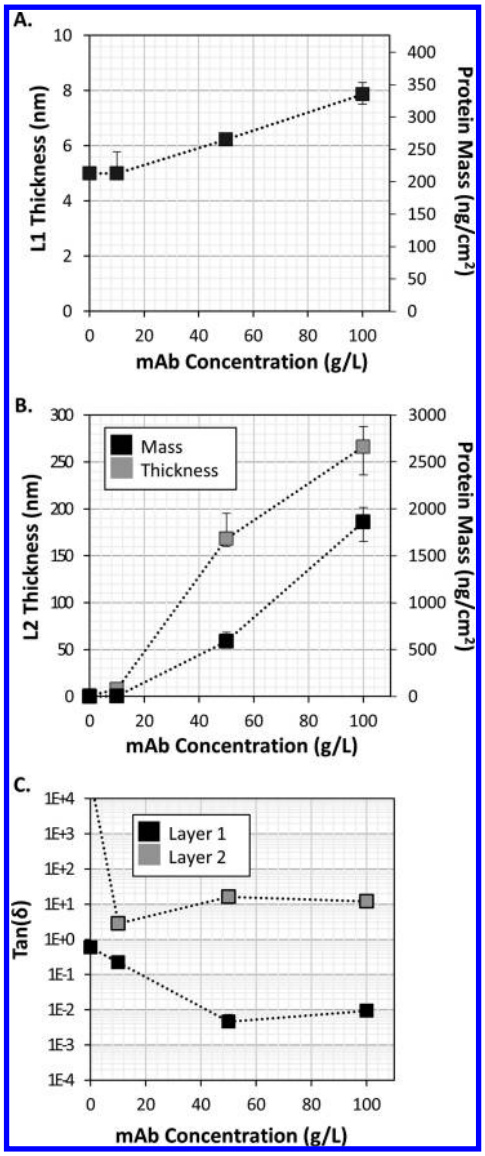

Figure 6. Physical properties of the adsorbed mAb layer and the neighboring environment determined using a two-layer Voigt viscoelastic model to fit the QCM-D data during mAb flow. (A,B) Thickness and mass of the primary layer and secondary layer, respectively. The mass of protein in layer 1 was calculated assuming that 30% of the layer was composed of mAb, and the mass of protein in layer 2 was calculated using protein fractions of 0.1, 0.7, 3.5, and 7.0% based on the solution densities for the 0.1, 10, 50, and 100 g/L mAb solutions, respectively. (C) Comparing the tan(δ) values for the primary and secondary layers as a function of mAb solution concentration. Error bars represent the parameter range where χ^2 is less than double that of the best fit.

The diffuse, liquid-like secondary (L2) layer also changed substantially as the mAb concentration was increased (Figure 6B). At 0.1 g/L, the modeled thickness of the secondary layer was negligible (thickness $\ll$ 1 nm), which is the one-layer Voigt model limit. The mass of protein in the secondary layer was also calculated to be $\ll$1 ng/cm^2. Increasing the mAb concentration from 10 to 50 and 100 g/L mAb increased the modeled L2 thickness from 8 to approximately 168 and 266 nm, respectively. The corresponding masses of protein within the layer were approximately 4.0, 588, and 1862 ng/cm^2 for the 10, 50, and 100 g/L mAb solutions, respectively. Although the thickness of and mass of protein in the secondary layer were quite large, the values for L2 tan(δ) demonstrate that the secondary layer behaves as a liquid for all of the mAb concentrations investigated. At 0.1 g/L, tan(δ) was $\gg$1000, showing again that the two-layer model had reduced the values of L2 to describe a one-layer limit. As the mAb concentration was increased, the modeled tan(δ) values ranged from 2.8 to 16, suggesting that the secondary layer was primarily liquid-like with some elastic behavior. Thus, a substantial fraction of the protein within the layer behaved as if it were within bulk solution. Furthermore, the calculated mass results demonstrate that while the secondary layer was calculated to be much thicker than the primary layer (>30× at 100 g/L) the mass of mAb contained in the secondary layer was much more comparable to the primary layer (~6× more mass in the secondary layer than the primary layer).

To determine the amount of mass adsorbed to the stainless steel sensor during buffer rinsing, the Sauerbrey model for rigid films was applied to the QCM-D data because the measured dissipation was negligible. There was little difference observed between the adsorbed mass for experiments performed at 0.1 and 10 g/L mAb (Figure 7). At 0.1 g/L, ~530 ng/cm^2 of mAb and trapped water was adsorbed to the sensor upon rinsing. This mass did not decrease over the 15 min buffer rinse interval. At 10 g/L, the adsorbed mass was initially ~580 ng/cm^2. This mass, on the other hand, decreased slightly in the first 2.5 min but remained constant after ~5 min at a value of ~520 ng/cm^2. For experiments performed at higher concentrations of 50 and 100 g/L, more mass was observed to be adsorbed to the stainless steel at the onset and conclusion of the rinsing step. Additionally, desorption was clear during the rinsing step. The initial masses for the adsorbed layers produced at 50 and 100 g/L were approximately 900 and 820 ng/cm^2, respectively, as the mAb solution was exchanged with buffer. For the layer produced at 50 g/L, slight desorption was observed for the first ~5 min and the mass decreased to ~760 ng/cm^2. More rapid desorption was observed with rinsing for the adsorbed layer produced at 100 g/L. Desorption occurred over the first ~5 min of rinsing for the 100 g/L mAb solution, and the final

DOI: 10.1021/acs.molpharmaceut.7b01127
Mol. Pharmaceutics XXXX, XXX, XXX−XXX

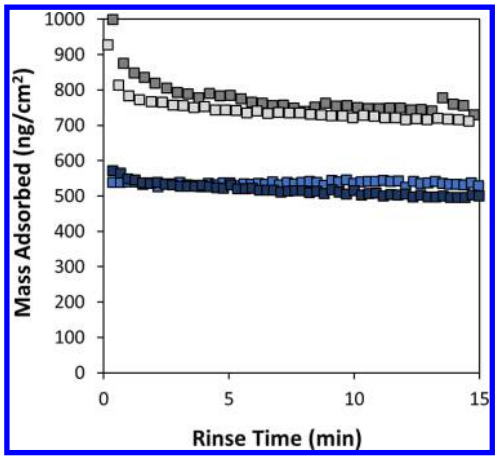

Figure 7. Remaining mass adsorbed to the stainless steel QCM-D sensor during the buffer rinse step calculated using the Sauerbrey model. The dark gray, light gray, dark blue, and light blue points represent the adsorbed mAb layers formed by the 100, 50, 10, and 0.1 g/L mAb solutions, respectively. Error bars are not provided because results are a direct calculation. Note that the total layer mass corresponds to roughly about 200−350 ng/cm^2 mass of protein.

mass of the layer was ∼790 ng/cm^2 after 15 min. The amount of mass adsorbed to the stainless steel sensor correlated well with the SVP data described above: at low concentration (e.g., 0.1 and 10 g/L mAb), the amount of adsorbed mass was substantially lower than that at high concentration (e.g., 50 and 100 g/L mAb). These relationships will be explored in detail in the discussion section.

As QCM-D identified that adsorption involves a primary layer (with negligible dissipation) and a secondary layer at high concentration (with substantial dissipation), we now turn to neutron reflectometry to investigate the structure of these layers. The dimensions of this mAb for the static homology structure were approximately 6.6, 13, and 16 nm, with the longest dimension representing the distance between the Fab and Fc. At a 0.1 g/L mAb solution concentration, a simple, ∼6 nm thick layer was observed (Figure 8A). The thickness and nSLD profile of the layer was like a monolayer of mAb molecules oriented flat at the interface (both Fab regions and the Fc region contacting the surface on one side). The surface coverage (area occupied) for this layer, however, was well below the surface coverage of a densely packed, native monolayer. At a 50 g/L mAb solution concentration, the volume fraction and structure of the adsorbed layer changed noticeably, with the % area occupied substantially increasing near the stainless steel interface (Figure 8B). As a result, the structure of the adsorbed mAb was no longer comparable to the modeled native mAb monolayer (Figure 8B). Interestingly, the thickness remained ∼6 nm, which suggests that the conformation of the adsorbed mAb changed rather than the molecules adopting a new orientation such as standing upright (e.g., with the variable domain of both Fab regions in contact with the interface). At 100 g/L mAb, the resulting structure and thickness of the adsorbed mAb layer were like the layer formed at a 50 g/L bulk mAb solution concentration. The structure of the primary layer was therefore found to vary with mAb solution concentration. Neutron reflectivity results do not clearly demonstrate the presence of a secondary layer. As the volume fraction of bulk protein solution is approximately 3.5 and 7% at 50 and 100 g/L, respectively, results indicate that the volume fraction of the secondary layer must be like the volume

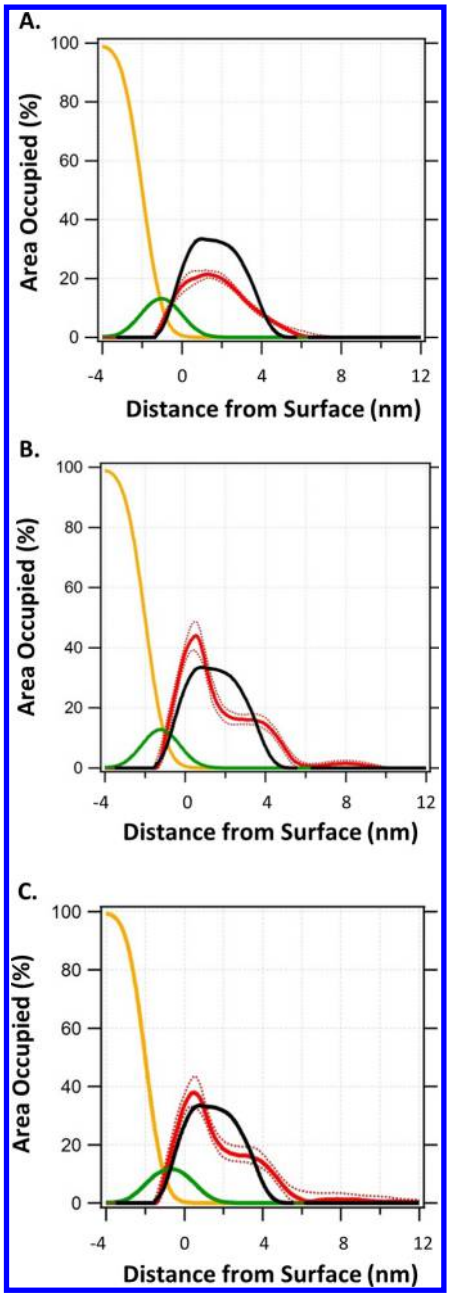

Figure 8. Structure of adsorbed mAb determined through modeling of neutron reflectivity data. The thick red trace represents the structure of the adsorbed mAb, and the thin, dashed red traces represent the 68% confidence interval for the fit. The black trace represents a theoretical profile for a densely packed monolayer where the mAb is oriented flat at the interface, the orange trace represents the stainless steel surface (gradual transition from solid to liquid arises due to surface roughness of the stainless steel), and the green trace is the calculated surface contamination. The bulk solution mAb concentrations are (A) 0.1, (B) 50, and (C) 100 g/L.

fraction of the mAb solution. If the volume fraction of the secondary layer was only a few percent more than the solution concentration and the secondary layer was very thick (e.g., >100 nm), it would be challenging to capture through neutron reflectivity because of weak contrast and high uncertainty at high Q_z values.

DOI: 10.1021/acs.molpharmaceut.7b01127
Mol. Pharmaceutics XXXX, XXX, XXX−XXX

DISCUSSION

SVP formation mechanisms mediated by solid−liquid interfaces can pose a challenge to the successful development of a therapeutic protein drug because interfaces such as stainless steel, glass, and/or plastics are present after the final filtration step during fill/finish. Several studies have demonstrated that solid−liquid interfaces may facilitate protein particle formation through desorption[13] or through shear/abrasion of protein adsorbed to solid surfaces.[41] In this work, the results of the previous studies are built upon by determining the structure of mAb adsorbed at the solid−liquid interface, modeling the viscoelastic properties of mAb near the interface, and by investigating the effect of flow (shear) and different interfaces (stainless steel and alumina) on SVP formation.

Particle formation observed in this study was primarily mediated by the solid−liquid interface. The evidence presented in this study suggests that shear disrupts protein adsorbed to the solid interface because (1) there was no air−water interface in the flow cell, (2) the flow cell with stainless steel produced more SVPs than the same flow cell with an alumina interface at the exact same shear rate (Figure 3A), (3) SVP formation was linear with concentration; the slope was much greater for the stainless steel interface than for the alumina interface, and (4) SVP formation was not substantially affected by flow rate (Figure 3B). In general, flow during biopharmaceutical manufacturing is not enough to cause protein aggregation on its own. For example, Bee et al. used a capillary rheometer to shear an IgG1 mAb solution at a rate of 250 000 s^{-1} and found that no aggregates were produced.[42] On the other hand, when a rotational rheometer was used to shear the mAb solution at 20 000 s^{-1}, detectable levels of protein aggregates were observed. Such differences can likely be attributed to the different interfaces present in each rheometer (e.g., protein can adsorb to an air−water interface in the rotational rheometer).[43]

Previous studies hypothesize that stainless steel particles, shed from pumps, act as a heterogeneous nucleation site for particle formation.[44] In this work, however, the stainless steel interface (in the flow cell) was not damaged (e.g., did not shed nanometer sized particles) throughout the experiment (Figure S5). SVP formation mediated at the solid−liquid interface could be one explanation for why SVPs often contain metal fragments/ions. For example, Wuchner et al. found that SVPs of a mAb contained trace amounts of silicon and aluminum and proposed that such elemental impurities were from the packaging materials.[45] Whether aggregates grew to SVPs at the interface or in bulk solution, however, remains unknown because particle detection was downstream and not in situ at the surface. The data in this study suggest that a substantial number of the SVPs that formed in the SS-RPP were caused by interfacial shear disrupting mAb adsorbed at the stainless steel interface. It is important to note that the SS-RPP represents a sufficiently complex system and SVP formation could also have been induced by many other factors such as shedding of stainless steel, cavitation, grinding of the piston, etc. Investigating all potential SVP formation mechanisms in the SS-RPP was beyond the intended scope of this article.

As stainless steel was demonstrated to mediate SVP formation as a function of mAb concentration, it was important to demonstrate how bulk solution mAb concentration affected the properties of mAb adsorbed to the solid−liquid interface. At bulk solution mAb concentrations ≥ 50 g/L, a two-stage adsorption process was observed and attributed to multiple adsorption layers. Initially, the mass of the primary layer at high concentration is comparable to the total mass adsorbed at low concentration. Over time, however, the primary layer continues to accumulate mass and becomes increasingly more rigid at bulk mAb solution concentrations ≥ 50 g/L. Simultaneously, the secondary layer forms over the primary layer with a thickness depending on the mAb solution concentration. Interestingly, the secondary layer remains liquid-like, suggesting that increased viscoelastic interactions at the solid−liquid interface (observed by QCM-D) can be attributed to increased protein−protein interactions. Shear modulus values acquired from QCM-D have previously been attributed to increased protein−protein interactions.[33,46,47] It is not clear whether interactions at the interface are enhanced above that in bulk solution. Measurements of linear viscoelastic moduli at high frequency in bulk solution, e.g., by diffusing wave spectroscopy, could be helpful to answer this question.

To obtain a better mechanistic understanding of subvisible particle formation at the solid−liquid interface, we now consider the mass of SVPs formed vs protein mass adsorbed at the solid−liquid interface. Unsurprisingly, adsorbed protein layers contained substantially more protein than the mass of protein calculated for the SVPs. In fact, only 1.4 ng/cm^2 of adsorbed protein would need to be shed to produce 20 000 spherical particles with a 2.5 μm diameter. This calculation was performed by assuming spherical SVP geometry (which substantially overestimates particle volume) and an internal particle volume fraction of 20% protein.[48] SVP populations of 10 000, 20 000, and 100 000 with a 2.5 μm diameter would have an approximate mass of 23, 46, and 230 ng, respectively. These numbers can be divided by the area of stainless steel in the flow cell (33 cm^2) to determine the mass of protein/area required to shed to produce X number of particles. Furthermore, it is also possible that some fraction of the SVPs produced during the shear cell experiments were shed from other solid interfaces present in the cell because the total number of particles formed in the flow cell represents the sum of particles shed from the primary interface (e.g., stainless steel or alumina) and from secondary interfaces (e.g., tubing, gasket, or connectors). However, the differences in SVP formation between the alumina and stainless steel demonstrate that the primary interface material had a substantial effect on this pathway compared to secondary interfaces (the largest secondary surface was a Si/SiOx wafer, which also had a surface area of 33 cm^2).

Specific comparisons are now used to further elucidate the relationship between desorption and SVP formation. The total mass adsorbed to the stainless steel QCM-D sensor at 0.1 g/L mAb was ∼520 ng/cm^2 throughout the rinsing step. In the flow cell, ∼28 000 SVPs formed after shearing the 0.1 g/L solution. Using the calculations from the previous paragraph, this corresponds to ∼2 ng/cm^2 if all of the particles came from the stainless steel interface. These calculated results confirm our experimental results that relatively large numbers of SVPs can be generated at the interface without observing a substantial loss in mass of the primary layer. At higher mAb concentrations (e.g., ≥50 g/L), a secondary adsorption event was observed leading to increased mass being bound to the QCM-D sensor. The large (∼250 ng/cm^2) difference in adsorbed mass on the stainless steel, after buffer exchange in the QCM-D flow cell, between the layers formed at 100 and 50 vs 10 and 0.1 g/L mAb could partially explain why 100 and 50 g/L mAb solutions produce more particles when exposed to flow after adsorbing to

DOI: 10.1021/acs.molpharmaceut.7b01127
Mol. Pharmaceutics XXXX, XXX, XXX−XXX

stainless steel. That is not meant to suggest that all of this additional mass is shed during flow but rather that a substantial amount of mass (~50 ng/cm^2) was observed to desorb over ~10 min (from 5 to 15 min) during 0.5 mL/min buffer flow. Such a decrease in mass would correspond to 700 000 spherical particles with a 2.5 μm diameter being produced in the shear cell.

It is important to be critical of comparisons between adsorbed mass and calculated SVP mass, which is almost always an overestimate of the amount of particulate protein.[48] First, the initial amount/rate of layer desorption at the onset of buffer flow was not discussed for the QCM-D rinsing experiments because the simultaneous exchange of background solutions could appear to be a change of mass. This is because the solution density and viscosity are changing as the solution exchanges in the flow cell. However, it is important to note that when considering initial desorption from the QCM-D sensor and the presence of secondary interfaces in the flow cell the true number of particles produced at a 50 g/L mAb solution concentration would be much higher than the calculated number of 700 000 if all of the material shed formed SVPs. On the other hand, it is important to note that the Sauerbrey model calculates the total bound mass and does not discriminate between mAb and bound or trapped water/buffer molecules, whereas the mass of SVPs was calculated considering only the mass of mAb in the particle. Despite the differences in the calculation of layer mass vs particle mass, the number of SVPs observed during the shearing studies (e.g., ~200 000 at 50 g/L) was still substantially lower than the mass desorbed from the QCM-D sensor (~31 ng/cm^2 between 5 and 15 min of rinsing, which suggests that most of the mass desorbing/shed from the interface did not produce SVPs. As no soluble aggregates were observed by SEC (Figure S2), the data suggest that shed material was not/did not remain as small aggregates. Therefore, most of the mass desorbed was instead either resolubilized or detached as smaller particles (i.e., at a size intermediate between those detected by SEC and MFI).

CONCLUSIONS

In this work, subvisible particle formation mediated by interfacial shear and adsorption to solid−liquid interfaces was investigated. Neutron reflectometry, QCM-D, and a flow cell were used to investigate the structure of NISTmAb adsorbed to stainless steel, the viscoelastic properties near the interface, and the effect of shear/different interface materials on SVP formation, respectively. Different solid−liquid interfaces were found to substantially affect SVP formation. For example, stainless steel caused significantly more SVPs to form during flow than alumina at high mAb concentrations (≥50 g/L). Interestingly, while higher interfacial shear rates produced more particles than lower interfacial shear rates, the results were not significant unless the differences in shear rates were extreme (e.g., 20 vs 25 000 s^{-1}). The concentration of the protein was also very important because more SVPs were produced at mAb high concentration in the presence of stainless steel. Several differences were noticeable at high mAb concentrations compared to lower mAb concentrations in the presence of stainless steel: (1) more material was adsorbed at the stainless steel interface, (2) conformational distortion of mAb in the primary layer occurred, and (3) increased protein−protein interactions near the interface were detected. After exchanging high-concentration mAb solution with histidine buffer, >50 ng/cm^2 mAb was observed to desorb over ~10 min. The calculated mass of 20 000 spherical SVPs with a 2.5 μm diameter corresponded to only 1.4 ng of mAb per cm^2 of interface. Thus, the mass of the SVPs detected in these samples was substantially less than the amount of material observed to desorb during flow. These results suggest that only a small fraction of desorbed mAb needs to be shed as particles to observe substantial SVP populations. These insights provide better mechanistic understanding as to why various material incompatibilities (e.g., IV bag material, pump material, container material) can result in high numbers of SVPs being detected in solution.

ASSOCIATED CONTENT

Supporting Information

The Supporting Information is available free of charge on the ACS Publications website at DOI: 10.1021/acs.molpharmaceut.7b01127.

Supplemental methods (including size exclusion chromatography and X-ray reflectivity) and supplemental Figures S1−S6 (including additional SS-RPP SVP data analysis, SVP concentration vs size for different interfaces, SVP concentration vs mAb concentration data fitting, size exclusion chromatography data, X-ray reflectivity data, and SVP concentration vs size for different interfacial shear rates) (PDF)

AUTHOR INFORMATION

Corresponding Author

*E-mail: steven.hudson@nist.gov.

ORCID

Steven D. Hudson: 0000-0002-3203-4833

Notes

NIST Disclaimer: Certain commercial materials and equipment are identified in this paper to adequately specify the experimental procedure. In no case does such identification imply recommendation or endorsement by the National Institute of Standards and Technology, nor does it imply that these are necessarily the best available for the purpose.

The authors declare no competing financial interest.

ACKNOWLEDGMENTS

This work was funded in part through a cooperative research and develop agreement (CRADA) between NIST and MedImmune entitled Measurement Development for Manufacturing and Biopharmaceuticals. The authors wish to acknowledge the NIST NanoFab group for preparing the stainless steel and alumina coated substrates. Dr. Kathryn Beers and Dr. Sara Orski from NIST are acknowledged for their support and guidance. Dr. Jai Pathak and Dr. William Leach from MedImmune are also recognized for their helpful discussions and guidance.

REFERENCES

(1) Pinholt, C.; Hartvig, R. A.; Medlicott, N. J.; Jorgensen, L. The Importance of Interfaces in Protein Drug Delivery - Why Is Protein Adsorption of Interest in Pharmaceutical Formulations? *Expert Opin. Drug Delivery* **2011**, *8*, 949−964.

(2) Ghazvini, S.; Kalonia, C.; Volkin, D. B.; Dhar, P. Evaluating the Role of the Air-Solution Interface on the Mechanism of Subvisible Particle Formation Caused by Mechanical Agitation for an Igg1Mab. *J. Pharm. Sci.* **2016**, *105*, 1643−1656.

DOI: 10.1021/acs.molpharmaceut.7b01127
Mol. Pharmaceutics XXXX, XXX, XXX−XXX

(3) Bee, J. S.; Schwartz, D. K.; Trabelsi, S.; Freund, E.; Stevenson, J. L.; Carpenter, J. F.; Randolph, T. W. Production of Particles of Therapeutic Proteins at the Air-Water Interface During Compression/Dilation Cycles. *Soft Matter* **2012**, *8*, 10329−10335.
(4) Lin, G. L.; Pathak, J. A.; Kim, D. H.; Carlson, M.; Riguero, V.; Kim, Y. J.; Buff, J. S.; Fuller, G. G. Interfacial Dilatational Deformation Accelerates Particle Formation in Monoclonal Antibody Solutions. *Soft Matter* **2016**, *12*, 3293−3302.
(5) Shieh, I. C.; Patel, A. R. Predicting the Agitation-Induced Aggregation of Monoclonal Antibodies Using Surface Tensiometry. *Mol. Pharmaceutics* **2015**, *12*, 3184−3193.
(6) Mehta, S. B.; Carpenter, J. F.; Randolph, T. W. Colloidal Instability Fosters Agglomeration of Subvisible Particles Created by Rupture of Gels of a Monoclonal Antibody Formed at Silicone Oil-Water Interfaces. *J. Pharm. Sci.* **2016**, *105*, 2338−2348.
(7) Mehta, S. B.; Lewus, R.; Bee, J. S.; Randolph, T. W.; Carpenter, J. F. Gelation of a Monoclonal Antibody at the Silicone Oil-Water Interface and Subsequent Rupture of the Interfacial Gel Results in Aggregation and Particle Formation. *J. Pharm. Sci.* **2015**, *104*, 1282−1290.
(8) Jones, L. S.; Kaufmann, A.; Middaugh, C. R. Silicone Oil Induced Aggregation of Proteins. *J. Pharm. Sci.* **2005**, *94*, 918−927.
(9) Thirumangalathu, R.; Krishnan, S.; Ricci, M. S.; Brems, D. N.; Randolph, T. W.; Carpenter, J. F. Silicone Oil- and Agitation-Induced Aggregation of a Monoclonal Antibody in Aqueous Solution. *J. Pharm. Sci.* **2009**, *98*, 3167−3181.
(10) Bee, J. S.; Davis, M.; Freund, E.; Carpenter, J. F.; Randolph, T. W. Aggregation of a Monoclonal Antibody Induced by Adsorption to Stainless Steel. *Biotechnol. Bioeng.* **2010**, *105*, 121−129.
(11) Bee, J. S.; Chiu, D.; Sawicki, S.; Stevenson, J. L.; Chatterjee, K.; Freund, E.; Carpenter, J. F.; Randolph, T. W. Monoclonal Antibody Interactions with Micro- and Nanoparticles: Adsorption, Aggregation, and Accelerated Stress Studies. *J. Pharm. Sci.* **2009**, *98*, 3218−3238.
(12) Tyagi, A. K.; Randolph, T. W.; Dong, A.; Maloney, K. M.; Hitscherich, C.; Carpenter, J. F. Igg Particle Formation During Filling Pump Operation: A Case Study of Heterogeneous Nucleation on Stainless Steel Nanoparticles. *J. Pharm. Sci.* **2009**, *98*, 94−104.
(13) Perevozchikova, T.; Nanda, H.; Nesta, D. P.; Roberts, C. J. Protein Adsorption, Desorption, and Aggregation Mediated by Solid-Liquid Interfaces. *J. Pharm. Sci.* **2015**, *104*, 1946−59.
(14) Carpenter, J. F.; et al. Overlooking Subvisible Particles in Therapeutic Protein Products: Gaps That May Compromise Product Quality. *J. Pharm. Sci.* **2009**, *98*, 1201−1205.
(15) Rosenberg, A. S. Effects of Protein Aggregates: An Immunologic Perspective. *AAPS J.* **2006**, *8*, E501−E507.
(16) Ratanji, K. D.; Derrick, J. P.; Dearman, R. J.; Kimber, I. Immunogenicity of Therapeutic Proteins: Influence of Aggregation. *J. Immunotoxicol.* **2014**, *11*, 99−109.
(17) Bi, V.; et al. Development of a Human Antibody Tolerant Mouse Model to Assess the Immunogenicity Risk Due to Aggregated Biotherapeutics. *J. Pharm. Sci.* **2013**, *102*, 3545−3555.
(18) Joubert, M.; et al. Highly Aggregated Antibody Therapeutics Can Enhance the Innate and Late-Stage T-Cell Immune Responses. *Abstr. Pap. Am. Chem. Soc.* 2012, *243*.
(19) Langdon, B. B.; Kastantin, M.; Walder, R.; Schwartz, D. K. Interfacial Protein-Protein Associations. *Biomacromolecules* **2014**, *15*, 66−74.
(20) McLoughlin, S. Y.; Kastantin, M.; Schwartz, D. K.; Kaar, J. L., Single-Molecule Resolution of Protein Structure and Interfacial Dynamics on Biomaterial Surfaces. *Abstr. Pap. Am. Chem. Soc.* 2014, *248*.
(21) Minton, A. P. Effects of Excluded Surface Area and Adsorbate Clustering on Surface Adsorption of Proteins. Ii. Kinetic Models. *Biophys. J.* **2001**, *80*, 1641−1648.
(22) Li, Y.; Roberts, C. J. Lumry-Eyring Nucleated-Polymerization Model of Protein Aggregation Kinetics. 2. Competing Growth Via Condensation and Chain Polymerization. *J. Phys. Chem. B* **2009**, *113*, 7020−7032.
(23) Kalonia, C.; Toprani, V.; Toth, R.; Wahome, N.; Gabel, I.; Middaugh, C. R.; Volkin, D. B. Effects of Protein Conformation, Apparent Solubility, and Protein-Protein Interactions on the Rates and Mechanisms of Aggregation for an Igg1monoclonal Antibody. *J. Phys. Chem. B* **2016**, *120*, 7062−7075.
(24) Andrews, J. M.; Roberts, C. J. A Lumry-Eyring Nucleated Polymerization Model of Protein Aggregation Kinetics: 1. Aggregation with Pre-Equilibrated Unfolding. *J. Phys. Chem. B* **2007**, *111*, 7897−7913.
(25) *State-of-the-Art and Emerging Technologies for Therapeutic Monoclonal Antibody Characterization Vol. 2. Biopharmaceutical Characterization: The Nistmab Case Study*. Schiel, J. E., Davis, D. L., Borisov, O. V., Eds.; American Chemical Society: Washington, DC, 2015.
(26) Dura, J. A.; et al. And/R: Advanced Neutron Diffractometer/Reflectometer for Investigation of Thin Films and Multilayers for the Life Sciences. *Rev. Sci. Instrum.* **2006**, *77*, 074301.
(27) Kirby, B. J.; Kienzle, P. A.; Maranville, B. B.; Berk, N. F.; Krycka, J.; Heinrich, F.; Majkrzak, C. F. Phase-Sensitive Specular Neutron Reflectometry for Imaging the Nanometer Scale Composition Depth Profile of Thin-Film Materials. *Curr. Opin. Colloid Interface Sci.* **2012**, *17*, 44−53.
(28) Ankner, J. F.; Majkrzak, C. F. In *Subsurface Profile Refinement for Neutron Specular Reflectivity*; SPIE, 1992.
(29) Heinrich, F.; Losche, M. Zooming in on Disordered Systems: Neutron Reflection Studies of Proteins Associated with Fluid Membranes. *Biochim. Biophys. Acta, Biomembr.* **2014**, *1838*, 2341−9.
(30) Kienzle, P. A.; Doucet, M.; McGillivray, D. J.; O'Donovan, K. V.; Berk, N. F.; Majkrzak, N. F. *Ga_Refl*. http://www.ncnr.nist.gov/reflpak (2000−2006).
(31) Donik, C.; Paulin, I.; Jenko, M. Influence of Mns Inclusions on the Corrosion of Austenitic Stainless Steels. *Mater. Tehnol* **2010**, *44*, 67−72.
(32) Kanazawa, K. K.; Gordon, J. G. Frequency of a Quartz Microbalance in Contact with Liquid. *Anal. Chem.* **1985**, *57*, 1770−1771.
(33) Patel, A. R.; Kerwin, B. A.; Kanapuram, S. R. Viscoelastic Characterization of High Concentration Antibody Formulations Using Quartz Crystal Microbalance with Dissipation Monitoring. *J. Pharm. Sci.* **2009**, *98*, 3108−3116.
(34) Rodahl, M.; Hook, F.; Krozer, A.; Brzezinski, P.; Kasemo, B. Quartz-Crystal Microbalance Setup for Frequency and Q-Factor Measurements in Gaseous and Liquid Environments. *Rev. Sci. Instrum.* **1995**, *66*, 3924−3930.
(35) Rodahl, M.; Kasemo, B. On the Measurement of Thin Liquid Overlayers with the Quartz-Crystal Microbalance. *Sens. Actuators, A* **1996**, *54*, 448−456.
(36) Sauerbrey, G. Verwendung Von Schwingquarzen Zur Wagung Dunner Schichten Und Zur Mikrowagung. *Eur. Phys. J. A* **1959**, *155*, 206−222.
(37) Voinova, M. V.; Rodahl, M.; Jonson, M.; Kasemo, B. Viscoelastic Acoustic Response of Layered Polymer Films at Fluid-Solid Interfaces: Continuum Mechanics Approach. *Phys. Scr.* **1999**, *59*, 391−396.
(38) Zolls, S.; Gregoritza, M.; Tantipolphan, R.; Wiggenhorn, M.; Winter, G.; Friess, W.; Hawe, A. How Subvisible Particles Become Invisible-Relevance of the Refractive Index for Protein Particle Analysis. *J. Pharm. Sci.* **2013**, *102*, 1434−1446.
(39) Fischer, H.; Polikarpov, I.; Craievich, A. F. Average Protein Density Is a Molecular-Weight-Dependent Function. *Protein Sci.* **2004**, *13*, 2825−2828.
(40) Singh, A.; Konovalov, O. Measuring Elastic Properties of a Protein Monolayer at Water Surface by Lateral Compression. *Soft Matter* **2013**, *9*, 2845−2851.
(41) Sediq, A. S.; van Duijvenvoorde, R. B.; Jiskoot, W.; Nejadnik, M. R. No Touching! Abrasion of Adsorbed Protein Is the Root Cause of Subvisible Particle Formation During Stirring. *J. Pharm. Sci.* **2016**, *105*, 519−529.
(42) Bee, J. S.; Stevenson, J. L.; Mehta, B.; Svitel, J.; Pollastrini, J.; Platz, R.; Freund, E.; Carpenter, J. F.; Randolph, T. W. Response of a

DOI: 10.1021/acs.molpharmaceut.7b01127
Mol. Pharmaceutics XXXX, XXX, XXX−XXX

Concentrated Monoclonal Antibody Formulation to High Shear. *Biotechnol. Bioeng.* **2009**, *103*, 936−943.
(43) Castellanos, M. M.; Pathak, J. A.; Colby, R. H. Both Protein Adsorption and Aggregation Contribute to Shear Yielding and Viscosity Increase in Protein Solutions. *Soft Matter* **2014**, *10*, 122−131.
(44) Tyagi, A. K.; Randolph, T. W.; Dong, A.; Maloney, K. M.; Hitscherich, C., Jr.; Carpenter, J. F. Igg Particle Formation During Filling Pump Operation: A Case Study of Heterogeneous Nucleation on Stainless Steel Nanoparticles. *J. Pharm. Sci.* **2009**, *98*, 94−104.
(45) Wuchner, K.; Buchler, J.; Spycher, R.; Dalmonte, P.; Volkin, D. B. Development of a Microflow Digital Imaging Assay to Characterize Protein Particulates During Storage of a High Concentration Igg1Monoclonal Antibody Formulation. *J. Pharm. Sci.* **2010**, *99*, 3343−3361.
(46) Saluja, A.; Badkar, A. V.; Zeng, D. L.; Nema, S.; Kalonia, D. S. Ultrasonic Storage Modulus as a Novel Parameter for Analyzing Protein-Protein Interactions in High Protein Concentration Solutions: Correlation with Static and Dynamic Light Scattering Measurements. *Biophys. J.* **2007**, *92*, 234−244.
(47) Saluja, A.; Kalonia, D. S. Nature and Consequences of Protein-Protein Interactions in High Protein Concentration Solutions. *Int. J. Pharm.* **2008**, *358*, 1−15.
(48) Kalonia, C.; Kumru, O. S.; Indira Prajapati, V.; Mathaes, R.; Engert, J.; Zhou, S. X.; Russell Middaugh, C.; Volkin, D. B. Calculating the Mass of Subvisible Protein Particles with Improved Accuracy Using Microflow Imaging Data. *J. Pharm. Sci.* **2015**, *104*, 536−547.

DOI: 10.1021/acs.molpharmaceut.7b01127
Mol. Pharmaceutics XXXX, XXX, XXX−XXX

Supporting Information

Protein Adsorption and Layer Formation at the Stainless Steel – Solution Interface Mediates Shear-Induced Particle Formation for an IgG1 Monoclonal Antibody

Cavan K. Kalonia[1,2], Frank Heinrich[3,4], Joseph E. Curtis[3], Sid Raman[2], Maria A. Miller[2], Steven D. Hudson[1]

[1]Material Measurement Laboratory, National Institute of Standards and Technology, Gaithersburg, MD 20899
[2]Formulation Sciences Department, MedImmune Inc., Gaithersburg, MD 20878
[3]NIST Center for Neutron Research, National Institute of Standards and Technology, Gaithersburg, MD 20899
[4]Department of Physics, Carnegie Mellon University, Pittsburgh, PA 15213

Supplemental Methods:

X-Ray Reflectivity

A Rigaku Smartlab X-Ray Diffractometer (Rigaku Corporation, Tokyo, Japan) was used to perform X-ray reflectivity measurements. The optical configuration was set to the standard parallel beam with medium resolution setup. Alignment of the X-ray source and detector was performed prior to conducting sample alignment. Sample measurements were performed by determining the reflectivity over a range of θ from 0 to 10˚. The data was modeled using GlobalFit software V2 (Rigaku Corporation).

Size Exclusion Chromatography

An Agilent 1100 high performance liquid chromatography (HPLC) system (Agilent Tecnhologies, Santa Clara, California) composed of a G1310A isocratic pump, a G1314A variable wavelength detector, and a G1328A injector was used with a TOSOH G3000WXL column (TOSOH Biosciences, Tokyo, Japan) to perform size-exclusion chromatography measurements (SEC). The mAb solution was diluted to 10 g/L and 250 µg of sample were injected onto the column. The mobile phase solution was pH 6.8 100 mM sodium phosphate buffer with 100 mM sodium sulfate and 50 µM sodium Azide.

Supplemental Figures:

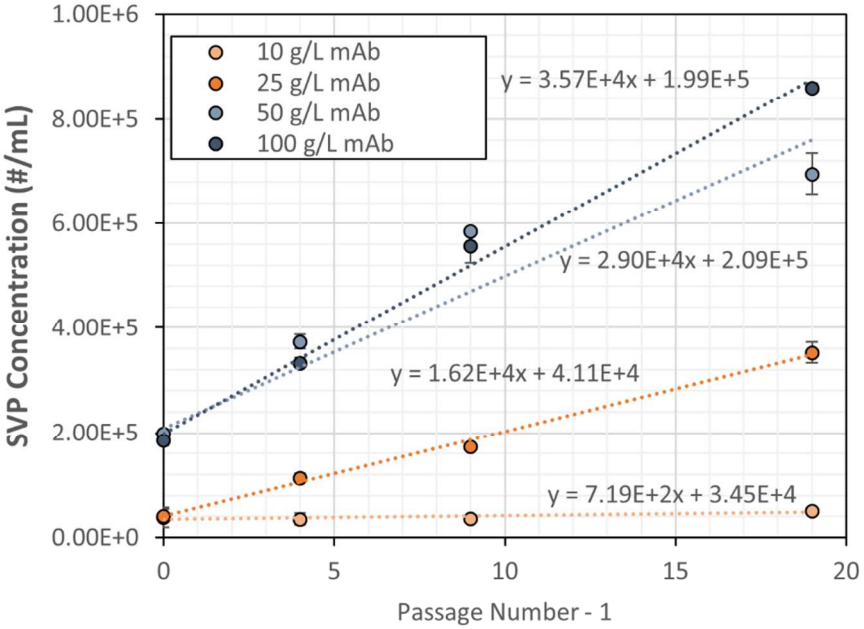

Supplemental Figure S1. The effect of additional passages of NISTmAb solutions through a stainless steel rotary piston pump. The light orange, orange, light blue, and dark blue circles represent the (10, 25, 50, and 100) g/L mAb solutions, respectively. Linear fits were used to

estimate the number of particles/passage produced after the initial pump passage. Error bars denote the standard error of the mean calculated from 6 measurements of the pumped solution. SVP were counted using flow cytometry.

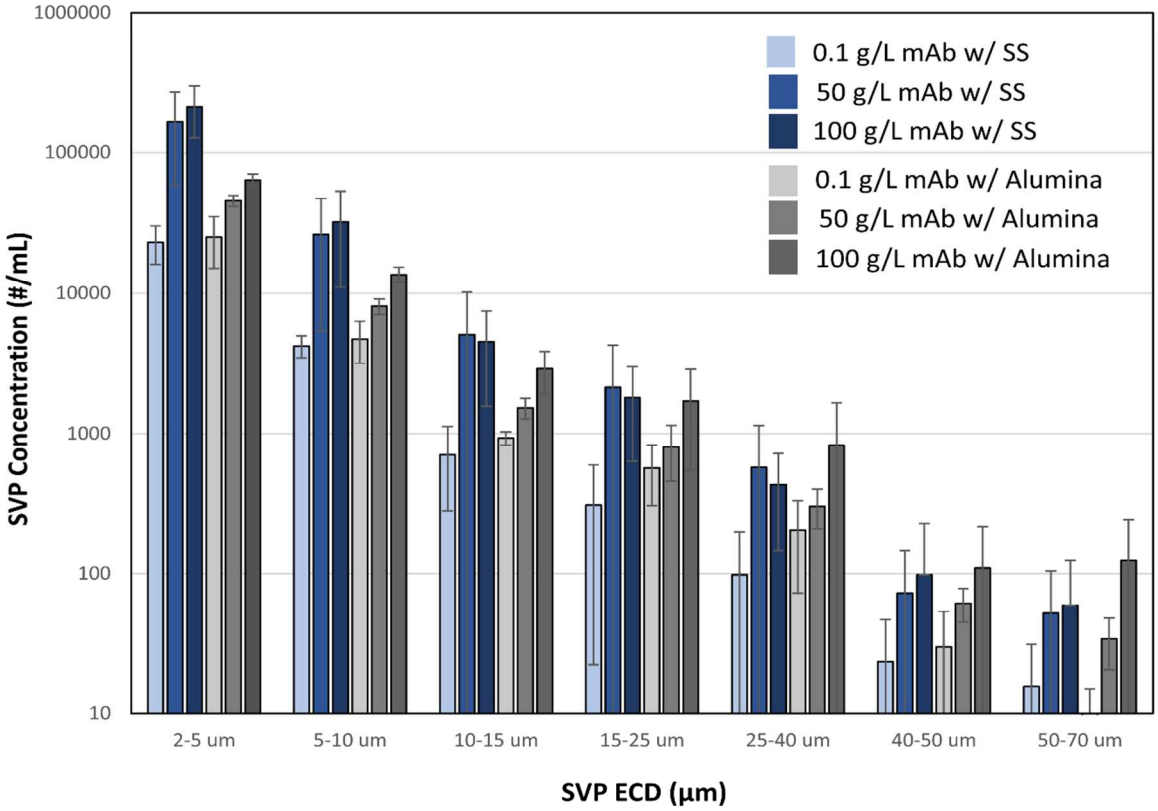

Supplemental Figure S2. **Size of subvisible particles detected after passage of NISTmAb solutions through a flow cell with different interface materials.** The total concentration of SVP vs. size in stressed NISTmAb solutions were counted using MFI. Error bars denote the standard deviation of 3 separate experiments. ECD = equivalent circular diameter.

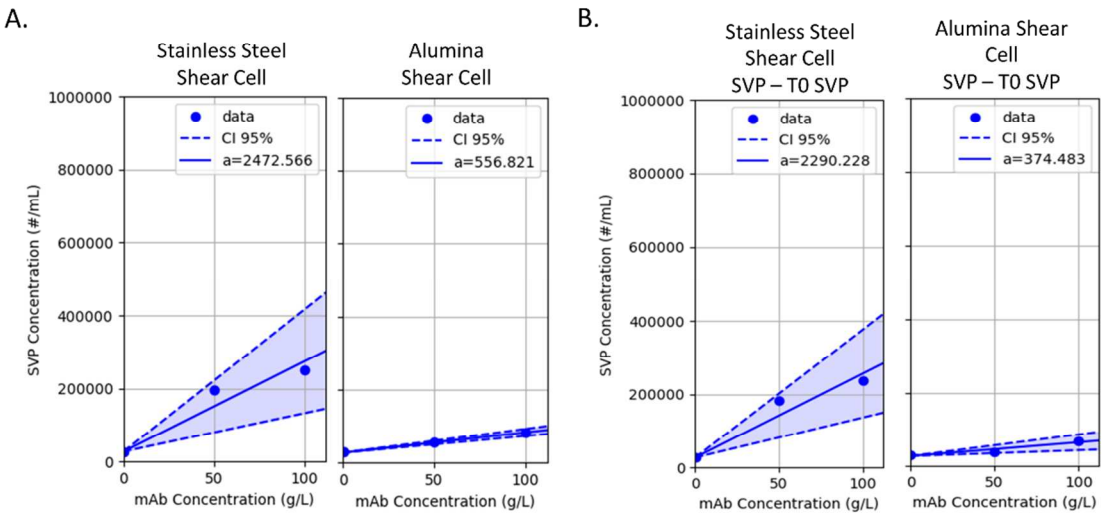

Supplemental Figure S3. The Slope of Average SVP Concentration vs. mAb Concentration for SVP Generated in the Shear Flow Cell. A) Comparison of the slope and 95% confidence interval between the shear flow cell equipped with the stainless steel interface (left) and the alumina interface (right). B) Comparison of the slope and 95% confidence interval for the stainless steel interface (left) and alumina interface (right) after the data has been normalized by average number of SVP in the control sample.

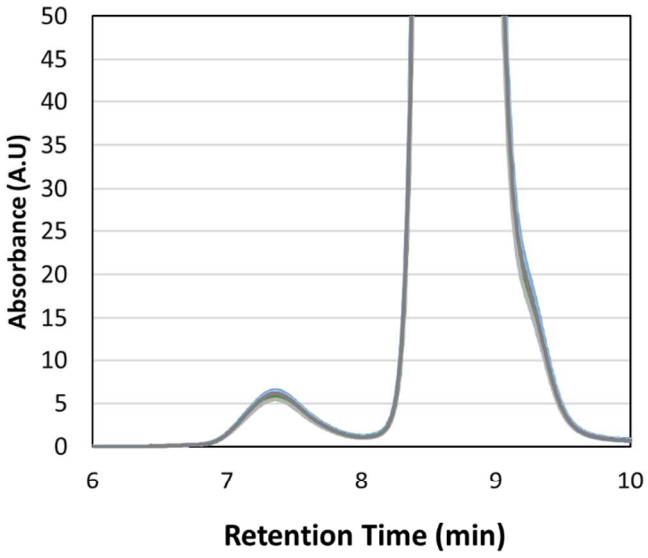

Supplemental Figure S4. Size exclusion chromatograms of stressed and unstressed NIST mAb samples. The figure includes the following overlaid data: 50 and 100 g/L NIST mAb (diluted to 10 g/L) after being sheared at (0.1, 2.0, or 120) mL/min. All samples were passed 3x times

through the flow cell. Samples sheared at 120 mL/min were also measured after being passed 10x times through the flow cell. The results are indistinguishable.

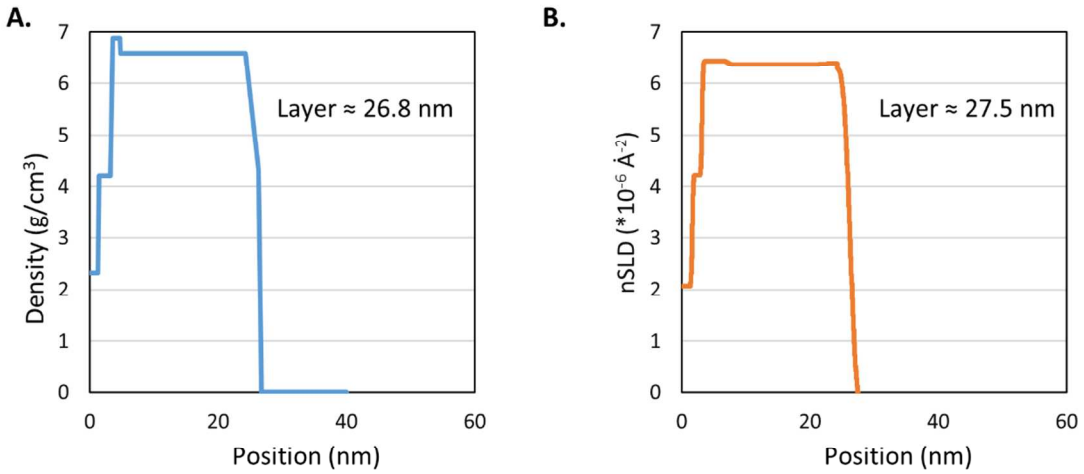

Supplemental Figure S5. Investigating the structural stability of sputtered stainless steel substrate using x-ray reflectivity. (Left) X-ray reflectivity data for the stainless steel substrate after adsorption experiments and cleaning with detergent. (Right) The scattering length density profile of a new substrate determined using neutron reflectivity. No significant differences are observed.

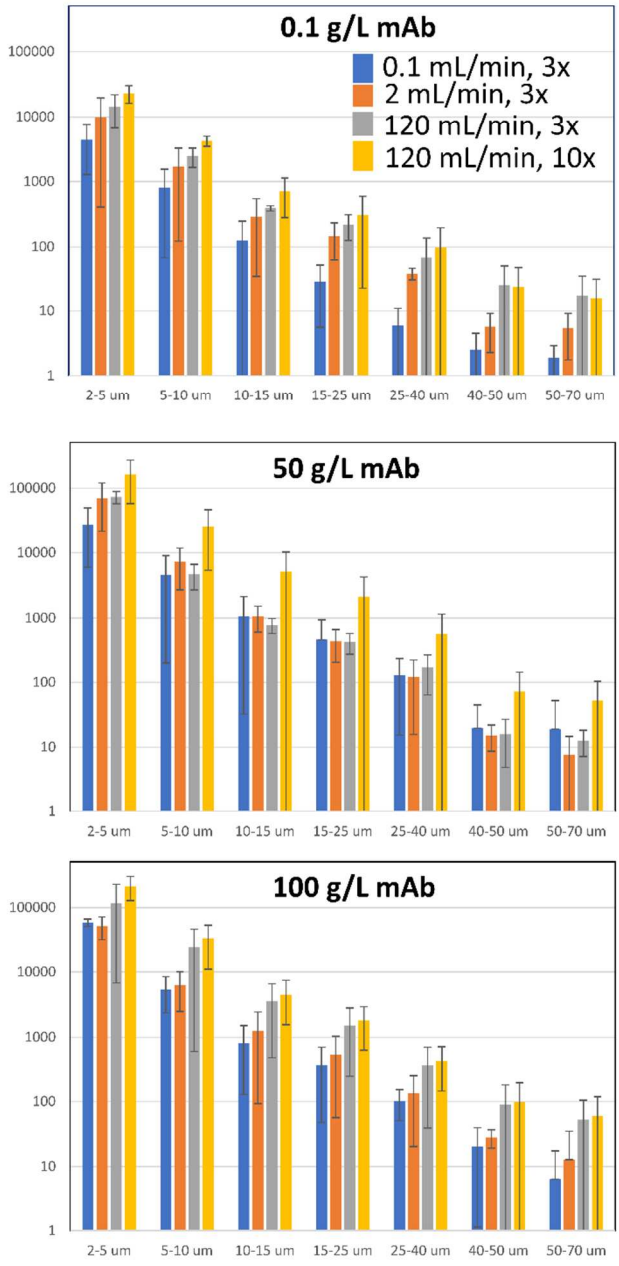

Supplemental Figure S6. Size of subvisible particles detected after passage of NISTmAb solutions through a stainless steel flow cell at different flow rates. The total concentration of SVP vs. size in stressed NISTmAb solutions were counted using MFI. Error bars denote the standard deviation of 3 separate experiments. ECD = equivalent circular diameter.